applied sciences

MDPI

Article

Oxidation of Zinc Microparticles by Microwave Plasma to Form Effective Solar-Sensitive Photocatalysts

Arsen Muslimov [1,*], Sergey Antipov [2], Makhach Gadzhiev [2], Anna Ulyankina [3], Valeria Krasnova [1], Alexander Lavrikov [1] and Vladimir Kanevsky [1]

[1] Federal Scientific Research Centre "Crystallography and Photonics" of Russian Academy of Sciences, Shubnikov Institute of Crystallography, 119333 Moscow, Russia; valeriya070707@inbox.ru (V.K.); lawrikow@gmail.ru (A.L.); kanev@crys.ras.ru (V.K.)
[2] Joint Institute for High Temperatures, Russian Academy of Sciences, 125412 Moscow, Russia; sappy78@mail.ru (S.A.); makhach@mail.ru (M.G.)
[3] Research Institute "Nanotechnologies and New Materials", Platov South-Russian State Polytechnic University (NPI), 346428 Novocherkassk, Russia
* Correspondence: amuslimov@mail.ru

Abstract: The presented work studies the processes of synthesis of ZnO microstructures using atmospheric-pressure microwave nitrogen plasma and investigates their photocatalytic activity in the processes of degradation of 2,4-dinitrophenol and the antibiotic ciprofloxacin when irradiated with sunlight. The work proposes an effective method for formation of photosensitive ZnO powders. Due to the features of plasma treatment in the open atmosphere of zinc metal microparticles, ZnO structures are formed with sizes from hundreds of nanometers to several micrometers with various micromorphologies. The lattice parameters of ZnO structures are characteristic of a hexagonal unit with a = 3.258 Å and c = 5.21 Å, volume 47.95 Å^3. The size of the crystallites is 48 nm. The plasma treatment was performed by means of a 2.45-GHz plasmatron at a power input of 1 kW in nitrogen flow at a rate of 1–10 L/min. Zn microparticles were injected into the microwave plasma at a mass rate of 20 g/min. High photoactivity was demonstrated (rate constants 0.036 min^{-1} and 0.051 min^{-1}) of synthesized ZnO structures during photo-degradation of 2,4-dinitrophenol and ciprofloxacin, respectively, when exposed to solar radiation. Photo-active structures of ZnO synthesized using microwave plasma can find application in processes of mineralization of toxic organic compounds. Structures of ZnO synthesized using microwave plasma can find application in processes of mineralization of toxic organic compounds, and also in scintillation detectors, phosphors.

Keywords: microwave plasma; zinc oxide; antibiotic; dinitrophenol; solar radiation; photocatalysts

check for updates

Citation: Muslimov, A.; Antipov, S.; Gadzhiev, M.; Ulyankina, A.; Krasnova, V.; Lavrikov, A.; Kanevsky, V. Oxidation of Zinc Microparticles by Microwave Plasma to Form Effective Solar-Sensitive Photocatalysts. *Appl. Sci.* **2023**, *13*, 12195. https://doi.org/10.3390/app132212195

Academic Editor: Young-Min Kim

Received: 19 October 2023
Revised: 6 November 2023
Accepted: 8 November 2023
Published: 10 November 2023

Copyright: © 2023 by the authors. Licensee MDPI, Basel, Switzerland. This article is an open access article distributed under the terms and conditions of the Creative Commons Attribution (CC BY) license (https://creativecommons.org/licenses/by/4.0/).

1. Introduction

All over the world today there is a shortage of clean water due to rapid population growth, environmental degradation, uncontrolled disposals from industrial enterprises, and the widespread introduction of chemical technologies in agriculture. Despite the widespread construction of modern treatment facilities, it is not possible to achieve complete wastewater treatment. This is due to the presence of difficult-to-oxidize organic pollutants, the most common of which are phenol-containing substances and antibiotics. Traditional treatment methods include mainly biological treatment and a number of physicochemical methods such as adsorption, ion exchange, and reverse osmosis. The disadvantages of these methods include the non-destructive nature of cleaning, high energy and operating costs, low efficiency, and the generation of large amounts of waste. In recent years, environmentally friendly and energy-efficient advanced oxidation technologies have been actively developed, among which photocatalysis (PC) occupies an important place [1,2]. An important advantage of PC is the possibility of oxidation at relatively low concentrations of pollutants [3], which is important for the mineralization of toxic organic

pollutants with low maximum permissible concentrations. The efficiency of PC is determined by the efficiency of formation and separation of photo-charges. For a long time, the main photocatalyst produced on an industrial scale was titanium dioxide (TiO_2) from Degussa (P-25) [4]. The disadvantage of TiO_2 is its significant band gap (Eg = 3.2 eV) and its maximum photocatalytic activity when irradiated with ultraviolet (UV) light. Ultraviolet radiation makes up only 5–7% of solar radiation. At the same time, visible radiation makes up about 45% and the search for photocatalysts active in the visible region is very relevant. A huge number of works are devoted to heterostructural and composite photocatalysts exhibiting activity in the visible region [5–10]. Despite individual studies demonstrating the effectiveness of hybrid photocatalysts, the traditionally utilized TiO_2 still remains the most popular. This is due to the lack of economically accessible technology for mass production of hybrid photocatalysts. As an alternative to TiO_2, ZnO [11,12], which is not inferior in efficiency and availability, has recently been actively studied. Despite the similarity of the band gap of ZnO (3.37 eV) with TiO_2 (3.2 eV), a distinctive feature of the band structure of ZnO is the presence of isolated energy levels in the band gap associated with point defects, mainly oxygen vacancies [13]. With a significant increase in the concentration of vacancies, photosensitivity can expand into the visible region of the spectrum. Dislocations are an additional source of levels in forbidden zones. The band structure is distorted around the dislocation core and a level is introduced closer to the center of the band gap. In n-type crystals, which include ZnO, dislocations can capture electrons and prevent their recombination. The highest concentration of defects is observed in crystals synthesized under conditions that are far from ideal: high saturation, unstable temperature gradient, and chaotic influx of atoms. Such conditions can be created using plasma synthesis of metal–oxide structures [14]. Plasma synthesis using gas-discharge plasma is not only energy-efficient but also has high productivity. Of greatest interest is the microwave (MW) discharge at atmospheric pressure, which has a much higher charge density and, consequently, greater reactivity compared to other discharges at the same power. In some types of atmospheric pressure discharges (corona, spark, and arc), plasma is "contaminated" by the material of internal discharge electrodes. This can be avoided for microwave discharges excited in chambers in the absence of direct contact with the metal electrodes, which is of fundamental importance in the generation of high-purity plasma. It should be noted that the possibility of using microwave plasma for the synthesis of photocatalytically active ZnO tetrapods was previously studied in [15]. However, the authors pay attention only to plasma regions in which the conditions for the formation of ZnO tetrapods are realized. This approach generally limits the performance of the photoactive ZnO catalyst. It seems to us that loading zinc metal powder directly into the gas transportation system is an important technological solution. Thus, the residence time of zinc metal in the plasma increases. Considering the plasma temperature of several thousand Kelvin, one can expect the instantaneous evaporation of zinc and the formation of individual ZnO elements with a wide range of sizes and different micromorphologies. It should be noted that micron-sized particles injected into a gas-discharge plasma become centers of recombination of plasma electrons and ions (sometimes a source of electrons owing to thermo-, photo-, and secondary electron emissions) and acquire a negative electric charge because of the greater mobility of electrons. In this case, the microparticle charge can reach significant values of up to 10^3–10^5 electron charges [16,17]. Owing to electrostatic interaction, particles of the same charge sign experience mutual Coulomb repulsion, which prevents them from sticking together and forming agglomerates. As a result, the form of individual ZnO elements with a large variation in size and different micromorphology with a developed surface can be expected. In order to enhance the photosensitivity of ZnO powder in the visible region, one can resort to nitridation of ZnO [18]. For this purpose, it is possible to utilize nitrogen as a buffer plasma-forming gas.

In the presented work, the processes of synthesis of ZnO structures using microwave plasma were studied and their photocatalytic activity in the processes of degradation of 2,4-dinitrophenol and the antibiotic ciprofloxacin under irradiation with sunlight was investigated.

2. Materials and Methods

2.1. Materials and Sample Preparation

For the experiment, zinc powders (99.98% purity) 30–40 μm mean particle size provided by OCHV, Russia, were utilized. The waveguide microwave atmospheric-pressure plasmatron was utilized for ZnO plasma synthesis (Figure 1).

To mix the powder with working gas, a simple transparent sealed container with visual control was constructed. Zinc powder was poured from the container into the discharge tube from the gas supply side and passed through the microwave discharge region inside the waveguide. Next, the particles of the treated Zn powder were collected through the open end of the discharge tube into a quartz cup. Zn microparticles were injected into the microwave plasma at a mass rate of 20 g/min. To organize the injection of microparticles into a discharge, several features of the microwave discharge at atmospheric pressure should be considered. Commonly, to maintain the stability of the discharge and isolate it from the walls of the discharge tube, various schemes for gas jet "swirling" are utilized. However, when solid dispersed particles are injected into the gas flow, they are centrifugally ejected from the central region onto the tube wall. To reduce the deposition of powder onto the walls, plasma-forming gas was introduced without swirling.

We utilized the microwave plasmatron developed on the basis of a 2.45-GHz magnetron with an output power of 1.1 kW. Unlike microwave plasmatrons of a "classical" design, our plasmatron is constructed using the simplified scheme "power supply–magnetron–waveguide–gas-discharge device–load". The WR-340 waveguide was fabricated from a stainless-steel rectangular profile. At the end of the waveguide, there is a resonant water load. In the middle of the wide walls of the waveguide central part, two pipe nozzles for the gas discharge device input were coaxially welded. A dielectric (quartz) tube with an internal diameter of 3 cm was placed through the perpendicular to the waveguide wide wall. A volumetric atmospheric-pressure stationary gas discharge was excited in the tube by microwaves inside the waveguide operating in the H_{10} mode. Thus, the tube acted as a plasma–chemical reactor in which microwave plasma was generated through which the plasma-forming gas flowed along with the dispersed particles being treated. High-purity nitrogen (99.998%) was utilized as the plasma-forming gas, and was introduced into the tube at a flow rate of 1–10 L/min.

To operate the magnetron, a high-voltage power supply circuit, which provides up to 3 kW of continuous output power from the magnetron, was utilized. The microwave discharge in a continuous wave (CW) regime can be obtained with the help of 'seed' ionization using a thin metal wire tip brought into the tube.

(**a**)

Figure 1. *Cont.*

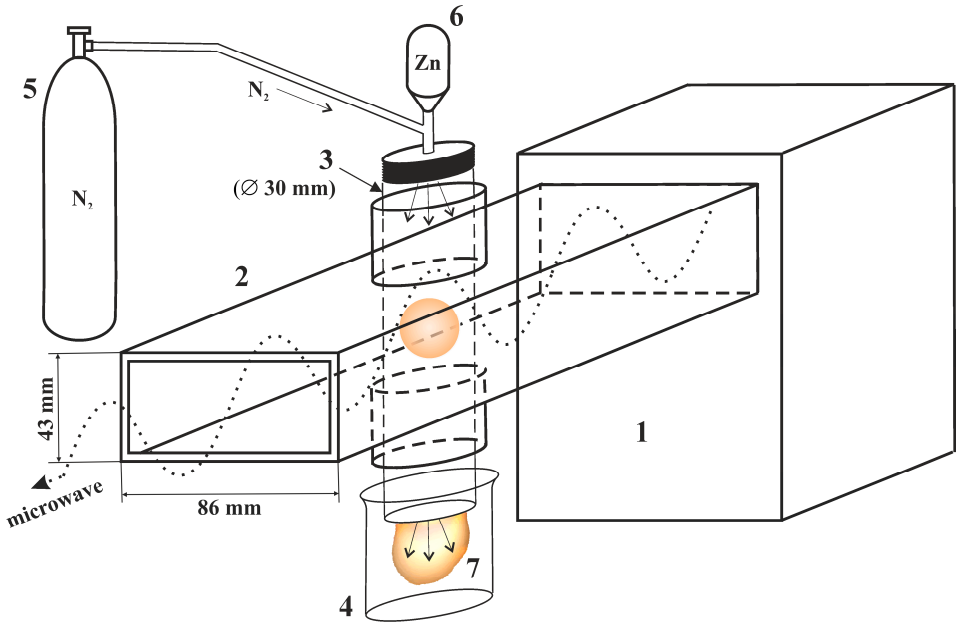

Figure 1. Microwave plasmatron image (**a**) and Scheme (**b**) of the experimental setup with the plasmatron: 1—microwave unit with 2.45-GHz magnetron, 2—rectangular waveguide, 3—quartz tube, 4—quartz cup, 5—N_2 gas cylinder, 6—container with Zn powder, and 7—microwave plasma flame with synthesized ZnO.

2.2. Testing

For microscopic studies, the JCM-6000 (JEOL, Tokyo, Japan) desktop scanning electron microscope (SEM) equipped with an energy dispersive X-ray (EDX) microanalyzer was utilized. X-ray studies were carried out on an X'PERTPRO diffractometer (PANalytical, Almelo, The Netherlands) in the Bragg–Brentano "reflection" geometry using CuK_α radiation (λ = 1.54 Å) with a Ni β-filter. Previously, the powder was thoroughly rubbed. X-ray photoelectron spectroscopy (XPS) utilizing the Specs spectrometer (Specs, Berlin, Germany) equipped with Al and Mg anodes was utilized to determine the chemical composition of the surface layer and to measure the valence band of the samples. The spectrometer is metrologically verified. In this work, we utilized Al anode excitation. The anode material was chosen in such a way that the useful signal did not overlap with the Auger lines. The spectra were recorded in the binding energy range from 0 to 1200 eV. The binding energies were calibrated over the C-C line of the C1s spectrum (E_q = 284.6 eV). The etching was conducted with argon ions with energy of 4 keV for 2 min. To determine the band gap by UV/VIS spectroscopy, a spectrometric complex based on the MDR-41 monochromator (NPO Spektr, Novocherkassk, Russia) was utilized. The material powder was poured onto a special holder and compacted thoroughly. Diffuse reflectance spectra were taken in the wavelength range of 200 to 500 nm.

To study the photocatalytic activity of the synthesized materials, ZnO powder (25 mg) was placed in aqueous solutions of 2,4-dinitrophenol (DNP) and ciprofloxacin (CIP) (volume 50 mL with a concentration of 5 mg/L), stirred in the dark for 30 min, then the suspension was irradiated with light with constant stirring. A solar radiation simulator (xenon lamp, 100 mW/cm^2) was utilized as a light source. The DNP concentration was determined spectrophotometrically based on the absorption maximum at 358 nm (Shimadzu UV-1800 spectrophotometer).

3. Results

Let us describe the advantages of the microwave plasma method for the synthesis of ZnO structures. In some types of atmospheric-pressure discharges (corona, spark, and arc), the plasma is inevitably "contaminated" by the material of the internal discharge

electrodes. This can be avoided using dielectric tubes that cross the waveguide. Since in this case there are no electrodes or direct contact of the plasma with the conductive parts of the gas-discharge device, this type of discharge is called "electrodeless". This characteristic is fundamental for generation of high purity plasmas.

It should be emphasized that when it comes to the efficiency of a discharge device, it is necessary to consider the materials of all internal elements that may be exposed to plasma particles. Energy losses due to interaction with the electrode metal, even if this does not lead to noticeable contamination of the treated materials, reduce the efficiency of the reactor. Utilizing a microwave plasmatron for material plasma modification renders it possible to combine the advantages of pure electrodeless discharge with the convenience of electromagnetic energy supply through waveguides [19].

In our method, the powder was injected into the discharge tube from the side of the gas supply. This led to intensive plasma treatment because the particles passed through both the discharge zone in the waveguide and the region of the plasma jet (plasma flame) behind the exit of the branch pipes. Without particles, a microwave plasmatron of a "classical" electrodeless design generates atmospheric-pressure plasma with a gas temperature of several thousand degrees. From the results of spectral diagnostics of a microwave discharge plasma in nitrogen flow, it is known that at a power input of about 1 kW the gas temperature on the axis of the discharge tube is 5000–6000 K, while the concentration and temperature of electrons in the plasma are 10^{13} cm^{-3} and 1 eV, respectively [20].

3.1. ZnO Powder Characterization

According to electron microscopy data (Figure 2a), a morphologically heterogeneous crystalline precipitate is formed during synthesis. Among the individual elements of the precipitate, tetrapods, or hexagonal rods, can be observed. The structures range in size from hundreds of nanometers to a few micrometers. According to EDX (Table 1), the composition of the ZnO powder contained, in addition to the main components of zinc and oxygen, an atomic fraction of nitrogen of the order of 4%, which confirms the nitridization of the precipitate. The observed excess oxygen content is associated with water vapors and oxygen absorbed by the surface of ZnO structures as well as contained in the pores of ZnO powder. Diffraction reflections on the X-ray diffraction spectrum of oxidized zinc microstructures correspond to the hexagonal wurtzite structure of ZnO (JCPDS no. 05-0664). The most intense reflections are observed at 31.68 °, 34.35 °, and 36.16 °, corresponding to reflections from planes (100), (002), and (101) ZnO. The lattice parameter d is determined from the Bragg–Wulff equation:

$$2d * \sin(\theta) = \lambda, \quad (1)$$

where θ is the diffraction angle and λ is the wavelength of the utilized radiation.

Table 1. Concentrations (in %) of the main components of ZnO powder before photocatalysis according to EDX data.

Element	Zn	O	N
Quantity %	27.56	68.32	4.12

The sizes of coherent scattering regions (CSRs) in the samples under study were estimated using the Debye–Scherrer formula:

$$D = \frac{k \cdot \lambda}{\beta \cdot \cos\ \theta'} \quad (2)$$

where D is the average size of CSRs, which can be less than or equal to the grain size; k is the dimensionless particle shape coefficient (Scherrer constant); λ is the wavelength of copper X-ray radiation; β is the width of the reflection at half maximum; and θ is the diffraction angle. The lattice parameters of ZnO powder are characteristic of a hexagonal unit with

a = 3.258 Å and c = 5.21 Å, volume 47.95 Å^3. The a and c values are higher than that of ZnO standard (JCPDS card no. 05-0664): a = 3.249 Å and c = 5.205 Å, volume 47.58 Å^3. The sizes of the crystallites 48 nm were estimated from formula (2).

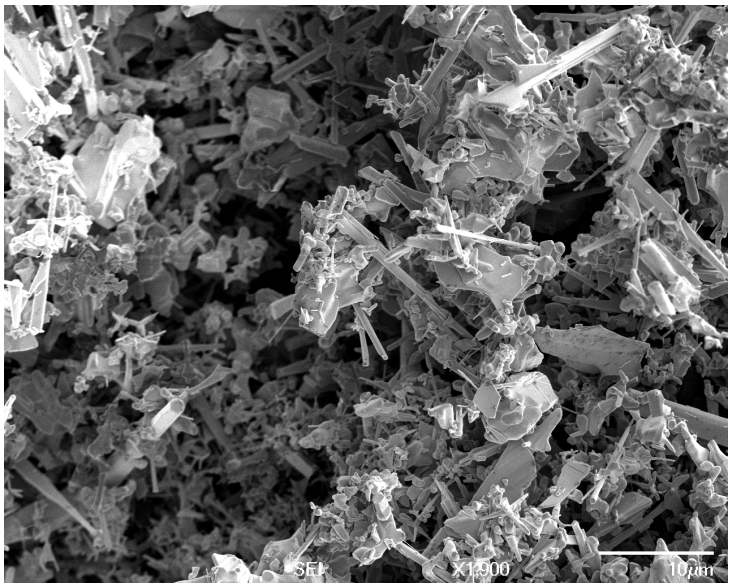

(**a**)

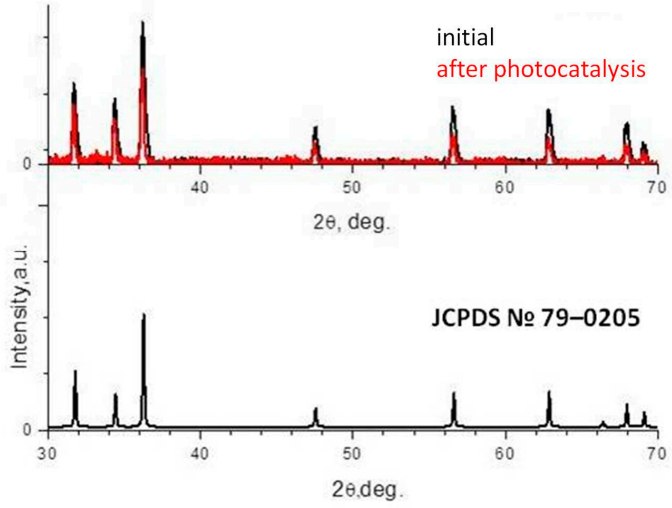

(**b**)

Figure 2. SEM images (**a**) and X-ray diffraction pattern (**b**) of ZnO powder. Scale bar: 10 μm.

Displacement may be due to an increase in the lattice parameter ZnO due to partial substitution of oxygen with nitrogen. Since the radius of nitrogen (1.46 Å) is greater than oxygen (1.38 Å), replacing oxygen with nitrogen in the ZnO lattice can cause it to deform. A similar effect was observed in [21]. According to XPS date (calculation was conducted for the spectra of Zn2p, O1s, and C1s), we calculated the concentrations of the main components of the powders (Table 2). It can be seen that the powder composition according to XPS was different from that obtained according to EDX (Table 1). The Zn-to-O atomic ratio, in this case, is closer to the stoichiometric value, however, there is an excess of zinc. For qualitative XPS analysis, the surface of the samples is previously etched, which results in surface cleaning. The excess of zinc found in the measurements is associated with a feature of the thermodynamically stable wurtzite phase of ZnO, in which oxygen vacancies and interstitial zinc are always present. These types of defects determine the electronic conductivity type ZnO. The presence of carbon (peak 285 eV corresponding to the C–O bond) is associated with hydrocarbon contamination of the surface, which is

difficult to remove. Of particular note is the absence of nitrogen in the surface layer, which was previously evident in the EDX data.

Table 2. Concentrations (in %) of the main components of ZnO powder before and after photocatalysis according to XPS data.

Sample	Zn	O	C	N
Initial	49.6	40.8	9.6	0
After photocatalysis	49.5	41.3	9.2	0

The melting and evaporation temperatures of zinc are 419.5 °C and 907 °C, respectively. As the particle size decreases, their thermodynamic characteristics change, and the melting and evaporation temperatures decrease. Under microwave discharge conditions, the gas temperature without particles is 5000–6000 K. Given the decrease in particle size after plasma treatment and their large size difference (Figure 2a), evaporation of Zn microparticles at the initial stage can be assumed. This assumption is supported by the presence of ZnO sharp structures, the growth of which is determined exclusively by zinc pairs. As noted above, micron-sized particles acquire a negative electrical charge due to incoming fluxes of electrons and ions from the surrounding plasma. Electrostatic repulsion of microparticles prevents their agglomeration. As a result, we observe a large variation in particle size and shape after plasma treatment. Zinc atoms enters a gaseous phase and reacts with active ionized nitrogen and oxygen diffusing from the open end of the quartz tube. If nitridization processes prevail at the initial stage. Oxidation processes prevail as the particles move to the open end of the tube. Zinc nitride phases have low stability at high temperatures in the presence of oxygen. It can be assumed that at the final stage there is a substitution of nitrogen atoms with oxygen atoms in the ZnO lattice in the direction from the surface deep into the sample. In addition, the enthalpy of ZnO formation is −350 kJ/mol and energy is released during zinc oxidation, which additionally heats the plasma. As a result, the distribution of temperature and other thermodynamic plasma parameters may be heterogeneous and a variety of ZnO forms is also associated with this. In addition, according to XRD (Figure 2b), there is no zinc metal in the synthesized ZnO powder. The presence of an oxide film allows complete oxidation of particles even at temperatures above the melting point of zinc [22], the diffusion of oxygen through the oxide layer limiting the liquid zinc in the central part of the particles.

3.2. Photocatalytic Properties of ZnO Powder

The photodegradation of DNP and CIP was evaluated under simulated solar light. Figure 3a,b represents absorption spectra of unirradiated (0 min) and irradiated DNP (Figure 3a) and CIP (Figure 3b) for 2, 5, 10, 20, 30, 40, and 60 min. The peculiarities of irradiation absorption are studied in [23,24]. As a result of irradiation of a semiconductor, surface photocatalytic reaction is initiated during which a photoelectron is promoted from the filled valence band to the empty conduction band of the semiconductor generating electron and hole pair (e−/h+). The photogenerated holes at the valence band can react with water to produce $OH^{\cdot}$ radical. The electron in the conduction band is taken up by the oxygen in order to generate anionic superoxide radicals. These powerful oxidizing agents attack adsorbed organic molecules non-selectively causing their mineralization [25]. Degradation of most organic compounds by photocatalysis may be described using a pseudo-first-order kinetic model for reactions that occur at the solid–liquid interface [26]. The ln (C/C_0) graph against time producing a linear line verifies that the reaction towards DNP and CIP follows the pseudo-first-order kinetic model. The apparent first-order rate constants (k_{app}) were 0.036 and 0.051 min^{-1} for DNP and CIP, respectively. During photocatalytic degradation of CIP antibiotic, complex organic molecules are converted into low molecular weight species. However, a tentative CIP photodegradation mechanism can include some pathways of the reaction: substitution of the F atom by the hydroxyl

group and the ring opening of the CIP molecule. The complete mineralization of CIP antibiotic occurs through the formation of CO_2, H_2O, and NO_3^- [27]. Oxidation of 2,4-dinitrophenol may occur through the ring opening by the attack of the OH radical. The overall degradation of 2,4-dinitriphenol results in the formation of smaller byproducts which may lead to mineralization [28].

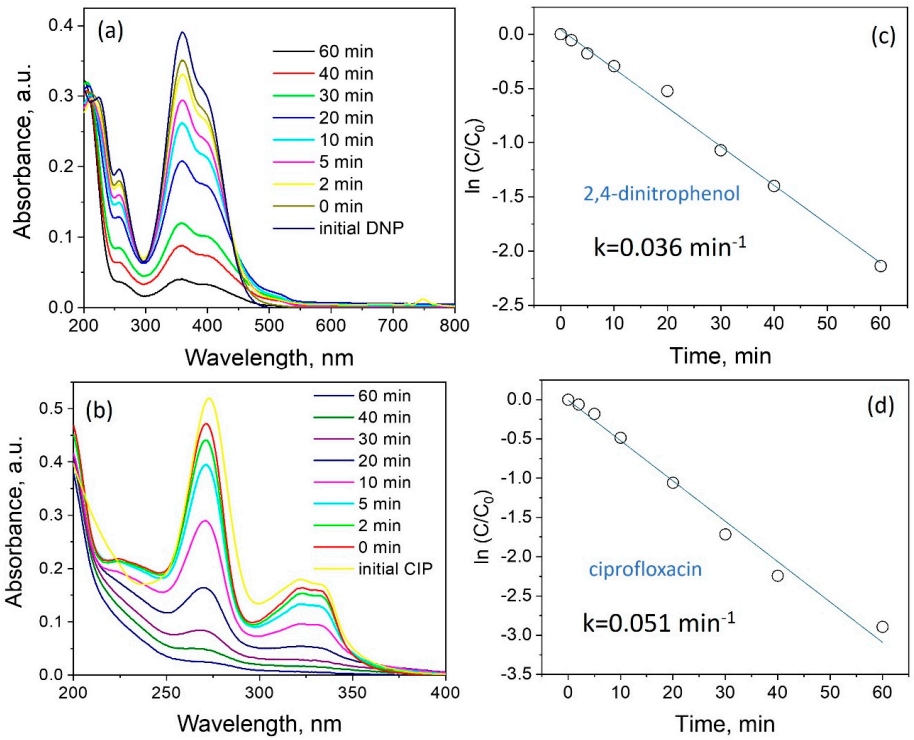

Figure 3. Photocatalytic performance of the synthesized ZnO powder: absorption spectra of DNP (**a**) and CIP (**b**) photodegradation under simulated solar light; kinetic linear fitting curves for DNP (**c**) and CIP (**d**) and corresponding apparent rate constants.

The results of this study are compared to those of similar papers that investigated the photodegradation of DNP and CIP (Table 3).

Table 3. Comparison of some of the recent literature reports on the photocatalytic degradation of CIP and DNP by various photocatalysts with our study.

Photocatalyst	Pollutant	Catalyst Dosage	Pollutant Concentration	Light Source (g L^{-1})	k_{app} (10^{-3} min^{-1})	Reference
ZnO/g-C_3N_4	CIP	0.5	5 mg L^{-1}	32 W compact fluorescent bulb	24	[29]
ZnO nanoparticles	CIP	0.6	12 mg L^{-1}	Natural sunlight, 221 W/m^2	13	[30]
TiO_2/SnO_2 nanocomposite	CIP	0.5	5 mg L^{-1}	Three UVC lamps with 35 W (253 nm)	28.2	[31]
carbon-nano-onion-functionalized ZnO tetrapods	DNP	2	0.1 mM	60 W tungsten bulb	18.34	[32]
Commercial P25	DNP	2	5 µM	266 W/m^2 Hg lamp	32	[33]
ZnO powder (microparticles)	CIP	0.5	5 mg L^{-1}	500 W Xenon lamp	51	This work
	DNP	0.5	5 mg L^{-1}	500 W Xenon lamp	36	This work

The mass photoactivity of commercial nanopowder photocatalysts is evidently higher than the one of the synthesized microparticles due to its lower particle size, higher surface area, and more active sites exposed for photoreaction [34]. However, on the one hand, the rate of collision and agglomeration is considerably higher for the lower particle size, leading to the formation of much larger agglomerates during the cycling test of the photocatalytic degradation. Particle aggregation and agglomeration influence the optical properties of materials and, therefore, their ability to absorb and scatter the incoming radiation, also affecting their photocatalytic activity. Moreover, the highly active nanoparticles are more vulnerable to photocorrosion when compared to microparticles [35]. On the other hand, nanoparticle synthesis requires more time and cost. Furthermore, it is not always possible to scale the nanoparticle synthesis process. In this work, the processing rate of Zn microparticles was 20 g/min and this can be increased in the future.

There may be several reasons for the high photoactivity of ZnO microstructures. First of all, it may be due to a structural factor. It was found [36] that nanorods have the greatest photocatalytic activity and this is associated with a high proportion of (100) texture. According to [37,38], in the plane (100) is the lowest energy of formation of defects, in particular, oxygen vacancies. According to XRD (Figure 2b), the ratio is I_{100}/I_{001}~1.27. Taking into account the large number of rod-like (001) structures of ZnO (Figure 2a), the value of the ratio 1.27 indicates the presence of a high fraction of (100) texture in the ZnO powder.

The next important factor is the adhesion levels of charge carriers in the ZnO band gap, which are associated with defects. Adhesion levels inhibit recombination of charge carriers and enhance photocatalytic activity. To determine the energy zone structure of the ZnO powder, XPS valence band spectra were obtained and the band gap was determined (Figure 4). The presence of energy state density near Fermi energy can be seen. These levels expand the photosensitivity of ZnO to the visible area. The VB_{max} energy was estimated to be 2.3 eV. Based on this, CB_{min} was estimated to be −0.9 eV. The levels in the band gap are mainly associated with oxygen vacancies and interstitial zinc [39]. For oxygen vacancies in the neutral V_O and 2+ charge states V_O^{2+}, a localized occupied state is recognized in the band gap at 2.5–2.6 eV and 0.9–1 eV below the conduction-band minimum [40], respectively, and this suggests the activity of ZnO tetrapods in the visible region of the spectrum.

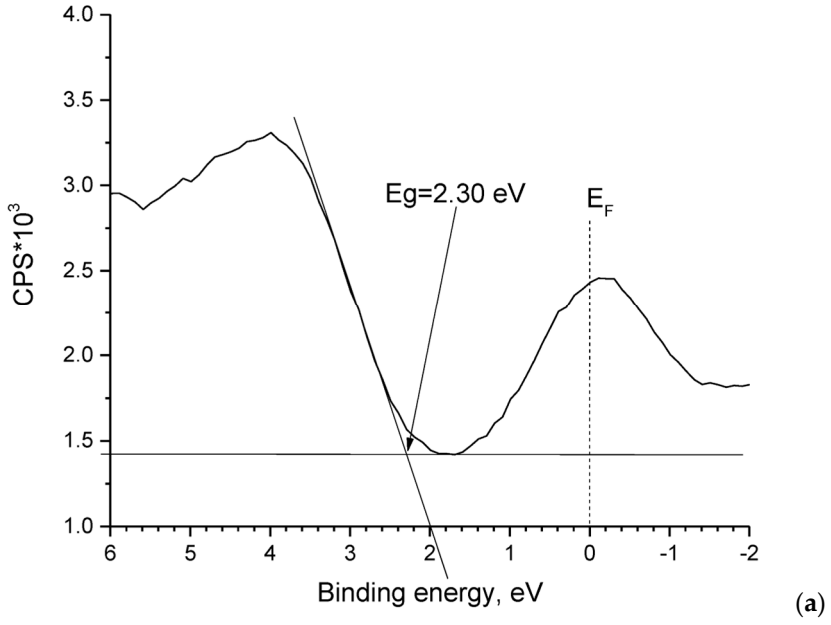

Figure 4. *Cont.*

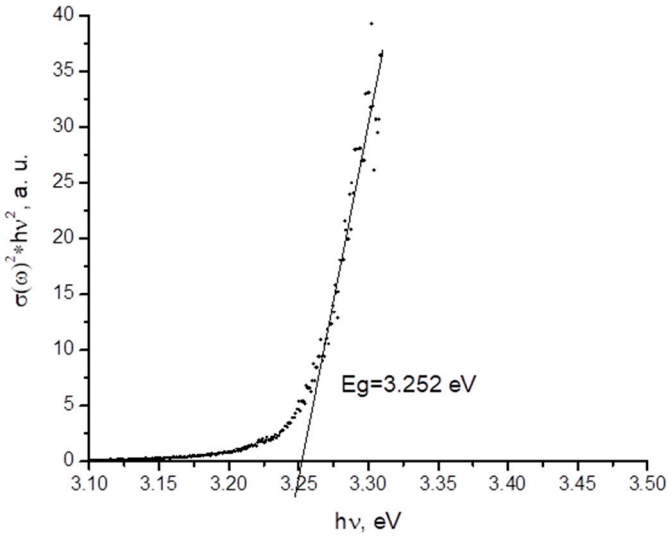

Figure 4. XPS valence band spectra (**a**) and Tauc's plots for the energy band gap (**b**) of ZnO powder.

This correlates with the structural features of ZnO powder and their effect on photocatalytic properties. As can be seen, the presence of nitrogen in the volume of ZnO structures does not lead to a narrowing of the band gap; however, energy levels associated with the nitrogen mixture in the band gap are present. For example, the energy state (0.3–0.4) eV below the bottom of the conduction zone is associated with the V_O-N defect complex [41]. There are also data on the acceptor level N2p above the valence zone by 0.76 eV [18].

3.3. Reproducibility of Photocatalyst Characteristics in Cyclic Processes

An important characteristic of the photocatalyst is the preservation of structural-phase properties, composition, and surface state. These characteristics affect the reproducibility of results in processes of photocatalytic degradation of organic pollutants. Samples of ZnO powder utilized in one CIP photodegradation cycle were examined. As shown by the XRD (Figure 2b) data, the structure-phase composition of the ZnO powder does not change. Figures 5 and 6 show the overview spectra of ZnO powder and individual components Zn2P3/2 (a) and O1s (b) before and after photocatalysis. It can be seen that the spectral lines coincide. In addition, the compositions found according to XPS data (Table 2) coincide within the limits of the error of the measurement.

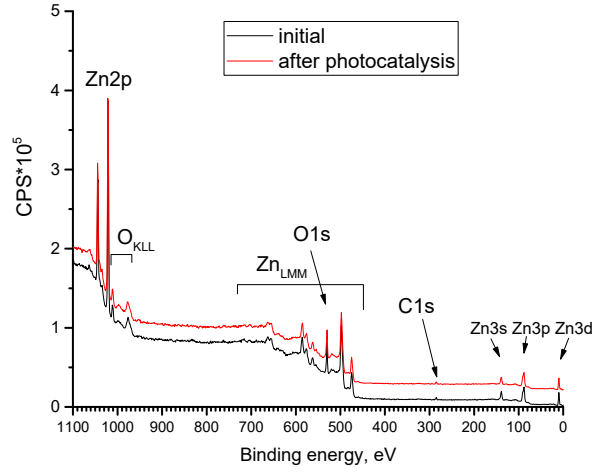

Figure 5. Panoramic XPS spectra of ZnO powder before and after photodegradation CIP.

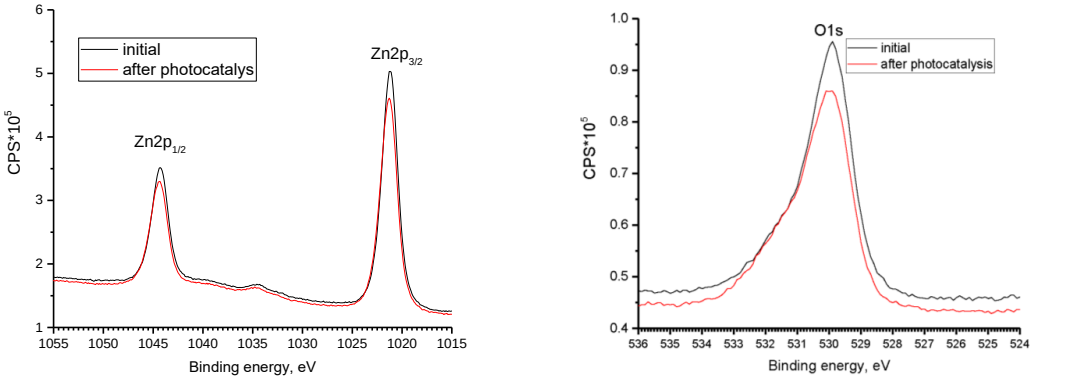

(**a**) (**b**)

Figure 6. XPS spectra $Zn2P_{3/2}$ (**a**) and O1s (**b**).

Analysis of features in the XPS spectra before and after photocatalysis also demonstrates the presence of the same components: 530.1 eV (the peak is characteristic of O^{2-} ions of the surface lattice oxygen in ZnO matrix), 531.3 eV (attributed to oxygen defects in the matrix of metal oxides, related to oxygen vaccines), and 532.6 eV (the band is related to the surface hydroxyl (Zn–OH) group).

4. Conclusions

The presented work studies the processes of synthesis of structures of ZnO using atmospheric pressure microwave nitrogen plasma and investigates their photocatalytic activity in the processes of degradation of 2,4-dinitrophenol and the antibiotic ciprofloxacin when irradiated with sunlight.

1. The work proposes an effective plasma method for formation of photosensitive ZnO powders. Zn microparticles were injected into the microwave plasma at a mass rate of 20 g/min;
2. Treatment of zinc metal powders using microwave nitrogen plasma has a number of advantages: a high gas temperature that promotes zinc evaporation and charging of microparticles by incoming fluxes of electrons and ions from the surrounding plasma that prevents the formation of agglomerates. Both of these factors contribute to the formation of ZnO structures ranging in size from hundreds of nanometers to several micrometers;
3. Study of the band gap parameters of ZnO structures using X-ray photoelectron spectroscopy demonstrates a high density of states near the Fermi level associated with defects contributing to the expansion of the photosensitivity range into the visible range;
4. High photoactivity was demonstrated (rate constants 0.036 min^{-1} and 0.051 min^{-1}) of synthesized ZnO structures during photodegradation of 2,4-dinitrophenol and ciprofloxacin, respectively, when exposed to solar radiation.

Structures of ZnO synthesized using microwave plasma can find application in processes of mineralization of toxic organic compounds.

In addition, ZnO microstructures can be utilized in scintillation detectors and phosphors, as well as being utilized as a binding component of strong composite materials.

Author Contributions: Conceptualization, A.M., S.A., A.U. and V.K. (Vladimir Kanevsky); methodology, A.M., A.L. and M.G.; validation, A.M. and M.G.; formal analysis, V.K. (Vladimir Kanevsky); investigation, S.A., A.U. and A.M.; resources, A.M., M.G., S.A., A.U. and V.K. (Valeria Krasnova); writing, A.M.; writing—review and editing, A.M.; visualization, A.M.; supervision, A.M., M.G. and V.K. (Valeria Krasnova); project administration, A.M. and V.K. (Valeria Krasnova); funding acquisition, A.M. and V.K. (Vladimir Kanevsky). All authors have read and agreed to the published version of the manuscript.

Funding: This research was performed in the frame of state assignments of the Ministry of Science and Higher Education of the Russian Federation for FSRC "Crystallography and Photonics" RAS (in part of structural studies of oxide powder), Federal State Budget Institution JIHT RAS (State Assignment No. 075-01129-23-00, in part of the development of plasma technologies), and within the Agreement with the Ministry of Science and Higher Education of the Russian Federation of 12.10.2021 №075-15-2021-1362 (in the part concerning the growth of ZnO microstructures as potential scintillation material).

Institutional Review Board Statement: Not applicable.

Informed Consent Statement: Not applicable.

Data Availability Statement: Data are contained within the article.

Acknowledgments: The authors are grateful to R.G. Valeev (the Center for Physical and Physico-Chemical Methods of Analysis, Study of the Properties and Characteristics of Surfaces, Nanostructures, Materials and Products, UdmFRC Ural Branch of the Russian Academy of Sciences) for their help in the study of samples by the method of XPS.

Conflicts of Interest: The authors declare no conflict of interest. The funders had no role in the design of the study; in the collection, analyses, or interpretation of data; in the writing of the manuscript; or in the decision to publish the results.

References

1. Ren, G.; Han, H.; Wang, Y.; Liu, S.; Zhao, J.; Meng, X.; Li, Z. Recent Advances of Photocatalytic Application in Water Treatment: A Review. *Nanomaterials* **2021**, *11*, 1804. [CrossRef] [PubMed]
2. Byrne, J.A.; Dunlop, P.S.M.; Hamilton, J.W.J.; Fernández-Ibáñez, P.; Polo-López, I.; Sharma, P.K.; Vennard, A.S.M. A Review of Heterogeneous Photocatalysis for Water and Surface Disinfection. *Molecules* **2015**, *20*, 5574–5615. [CrossRef] [PubMed]
3. Herrmann, J.-M. Heterogeneous photocatalysis: Fundamentals and applications to the removal of various types of aqueous pollutants. *Catal. Today* **1999**, *53*, 115–129. [CrossRef]
4. Matthews, R.; McEvoy, S. Destruction of phenol in water with sun, sand, and photocatalysis. *Sol. Energy* **1992**, *49*, 507–513. [CrossRef]
5. Mugumo, R.; Ichipi, E.; Tichapondwa, S.M.; Chirwa, E.M.N. Visible-Light-Induced Photocatalytic Degradation of Rhodamine B Dye Using a CuS/ZnS p-n Heterojunction Nanocomposite under Visible-Light Irradiation. *Catalysts* **2023**, *13*, 1184. [CrossRef]
6. Chen, H.; Hu, Y.; Ying, Z.; Xia, Y.; Ye, J.; Zhao, J.; Zhang, S. BiOI-SnO_2 Heterojunction Design to Boost Visible-Light-Driven Photocatalytic NO Purification. *Int. J. Environ. Res. Public Health* **2023**, *20*, 4009. [CrossRef]
7. Chowdhury, A.; Balu, S.; Lan, K.-W.; Wei-Chih Lee, L.; Yang, T.C.-K. Synergistic Effect of $BiVO_4$/P-g-C_3N_4 Heterojunction with Enhanced Optoelectronic Properties on Synthetic Colorants under Visible Light. *Colorants* **2023**, *2*, 426–442. [CrossRef]
8. Yan, X.; Ning, G.; Zhao, P. Enhanced Visible Light Photocatalytic Reduction of Cr(VI) over a Novel Square Nanotube Poly (Triazine Imide)/TiO_2 Heterojunction. *Catalysts* **2019**, *9*, 55. [CrossRef]
9. Wang, W.-Y.; Sang, T.; Zhong, Y.; Hu, C.-H.; Wang, D.-H.; Ye, J.-C.; Wei, N.-N.; Liu, H. Surfactant-Modified CdS/$CdCO_3$ Composite Photocatalyst Morphology Enhances Visible-Light-Driven Cr(VI) Reduction Performance. *Nanomaterials* **2022**, *12*, 3923. [CrossRef]
10. Yadav, A.A.; Hunge, Y.M.; Kang, S.-W. Visible Light-Responsive CeO_2/MoS_2 Composite for Photocatalytic Hydrogen Production. *Catalysts* **2022**, *12*, 1185. [CrossRef]
11. Mohamed, K.M.; Benitto, J.J.; Vijaya, J.J.; Bououdina, M. Recent Advances in ZnO-Based Nanostructures for the Photocatalytic Degradation of Hazardous, Non-Biodegradable Medicines. *Crystals* **2023**, *13*, 329. [CrossRef]
12. Ma, S.; Huang, Y.; Hong, R.; Lu, X.; Li, J.; Zheng, Y. Enhancing Photocatalytic Activity of ZnO Nanoparticles in a Circulating Fluidized Bed with Plasma Jets. *Catalysts* **2021**, *11*, 77. [CrossRef]
13. Alkauskas, A.; Pasquarello, A. Band-edge problem in the theoretical determination of defect energy levels: The O vacancy in ZnO as a benchmark case. *Phys. Rev. B* **2011**, *84*, 125206. [CrossRef]
14. Hanif, A.; Kim, Y.S.; Ameen, S.; Kim, H.G.; Kwac, L.K. Boosting the Visible Light Photocatalytic Activity of ZnO through the Incorporation of N-Doped for Wastewater Treatment. *Coatings* **2022**, *12*, 579. [CrossRef]
15. Heo, S.-G.; Jo, S.-I.; Jeong, G.-H. Revealing the enhanced photocatalytic properties of ZnO tetrapods produced by atmospheric-pressure microwave plasma jet system. *Curr. Appl. Phys.* **2023**, *46*, 46–54. [CrossRef]
16. Fortov, V.; Ivlev, A.; Khrapak, S.; Khrapak, A.; Morfill, G. Complex (dusty) plasmas: Current status, open issues, perspectives. *Phys. Rep.* **2005**, *421*, 1–103. [CrossRef]
17. Ishihara, O. Complex plasma: Dusts in plasma. *J. Phys. D Appl. Phys.* **2007**, *40*, R121. [CrossRef]
18. Koohgard, M.; Sarvestani, A.M.; Hosseini-Sarvari, M. Photocatalytic synthesis of unsymmetrical thiourea derivatives via visible-light irradiation using nitrogen-doped ZnO nanorods. *New J. Chem.* **2020**, *44*, 14505–14512. [CrossRef]

19. Moisan, M.; Sauve, G.; Zakrzewski, Z.; Hubert, J. An atmospheric pressure waveguide-fed microwave plasma torch: The TIA design. *Plasma Sources Sci. Technol.* **1994**, *3*, 584–592. [CrossRef]
20. Baltin, L.; Batenin, V.M.; Lebedeva, V.; Tsemko, N.; Devyatkin, I. Stationary microwave discharge in nitrogen at atmospheric pressure. *High Temp.* **1971**, *9*, 1019.
21. Lavand, A.B.; Malghe, Y.S. Synthesis, characterization and visible light photocatalytic activity of nitrogen-doped zinc oxide nanospheres. *J. Asian Ceram. Soc.* **2015**, *3*, 305–310. [CrossRef]
22. García, J.F.; Sánchez, S.; Metz, R. Complete Oxidation of Zinc Powder. *Valid. Kinet. Models* **2008**, *69*, 317–325. [CrossRef]
23. An, Z.; Huang, Y.; Zhang, R. High-temperature multispectral stealth metastructure from the microwave-infrared compatible design. *Compos. Part B Eng.* **2023**, *259*, 110737. [CrossRef]
24. Zheng, J.; Wei, X.; Li, Y.; Dong, W.; Li, X.; E, S.; Wu, Z.; Wen, J. Stretchable polyurethane composite foam triboelectric nanogenerator with tunable microwave absorption properties at elevated temperature. *Nano Energy* **2021**, *89*, 106397. [CrossRef]
25. Ajmal, A.; Majeed, I.; Malik, R.N.; Idriss, H.; Nadeem, M.A. Principles and mechanisms of photocatalytic dye degradation on TiO_2based photocatalysts: A comparative overview. *RSC Adv.* **2014**, *4*, 37003–37026. [CrossRef]
26. Hassan, N.; Jalil, A.; Fei, I.; Razak, M.; Khusnun, N.; Bahari, M.; Riwayati, Y.; Suprapto, S.; Prasetyoko, D.; Firmansyah, M.; et al. Vanadia as an electron-hole recombination inhibitor on fibrous silica-titania for selective hole oxidation of ciprofloxacin and Congo red photodegradation. *Chemosphere* **2023**, *338*, 139502. [CrossRef]
27. Bano, K.; Kaushal, S.; Lal, B.; Joshi, S.K.; Kumar, R.; Singh, P.P. Fabrication of CuO/ZnO heterojunction photocatalyst for efficient photocatalytic degradation of tetracycline and ciprofloxacin under direct sun light. *Environ. Nanotechnol. Monit. Manag.* **2023**, *20*, 100863. [CrossRef]
28. Rani, M.; Rachna; Yadav, J.; Shanker, U. Efficient degradation of nonylphenol and 2,4-dinitrophenol by sunlight responsive hexacyanocobaltates nanostructures. *Environ. Nanotechnol. Monit. Manag.* **2020**, *14*, 100325. [CrossRef]
29. Van Thuan, D.; Nguyen, T.B.; Pham, T.H.; Kim, J.; Chu, T.T.H.; Nguyen, M.V.; Nguyen, K.D.; Al-Onazi, W.A.; Elshikh, M.S. Photodegradation of ciprofloxacin antibiotic in water by using ZnO-doped g-C3N4 photocatalyst. *Chemosphere* **2022**, *308*, 136408. [CrossRef]
30. Mukherjee, I.; Cilamkoti, V.; Dutta, R.K. Sunlight-Driven Photocatalytic Degradation of Ciprofloxacin by Carbon Dots Embedded in ZnO Nanostructures. *ACS Appl. Nano Mater.* **2021**, *4*, 7686–7697. [CrossRef]
31. Costa, L.N.; Nobre, F.X.; Lobo, A.d.O.; de Matos, J.M.E. Photodegradation of ciprofloxacin using Z-scheme TiO_2/SnO_2 nanostructures as photocatalyst. *Environ. Nanotechnol. Monit. Manag.* **2021**, *16*, 100466. [CrossRef]
32. Park, S.J.; Das, G.S.; Schütt, F.; Adelung, R.; Mishra, Y.K.; Tripathi, K.; Kim, T.M. Visible-light photocatalysis by carbon-nano-onion-functionalized ZnO tetrapods: Degradation of 2,4-dinitrophenol and a plant-model-based ecological assessment. *NPG Asia Mater.* **2019**, *11*, 8. [CrossRef]
33. Mao, L.; Shen, J.; Ma, X.; Lan, Z.; Zhang, X. Effects of operational parameters on the photodegradation of 2,4-dinitrophenol in TiO2dispersion. *Desalination Water Treat.* **2014**, *56*, 744–751. [CrossRef]
34. Ohno, T.; Sarukawa, K.; Tokieda, K.; Matsumura, M. Morphology of a TiO_2 Photocatalyst (Degussa, P-25) Consisting of Anatase and Rutile Crystalline Phases. *J. Catal.* **2001**, *203*, 82–86. [CrossRef]
35. Toe, C.Y.; Scott, J.; Amal, R.; Ng, Y.H. Recent advances in suppressing the photocorrosion of cuprous oxide for photocatalytic and photoelectrochemical energy conversion. *J. Photochem. Photobiol. C Photochem. Rev.* **2018**, *40*, 191–211. [CrossRef]
36. Das, A.; Nikhil, S.K.; Nair, R.G. Influence of surface morphology on photocatalytic performance of zinc oxide: A review. *Nano-Struct. Nano-Objects* **2019**, *19*, 100353. [CrossRef]
37. Wang, M.; Zhang, Y.; Zhou, Y.; Yang, F.; Kim, E.J.; Hahn, S.H.; Seong, S.G. Rapid room-temperature synthesis of nanosheet-assembled ZnO mesocrystals with excellent photocatalytic activity. *CrystEngComm* **2012**, *15*, 754–763. [CrossRef]
38. Kislov, N.; Lahiri, J.; Verma, H.; Goswami, D.Y.; Stefanakos, E.; Batzill, M. Photocatalytic Degradation of Methyl Orange over Single Crystalline ZnO: Orientation Dependence of Photoactivity and Photostability of ZnO. *Langmuir* **2009**, *25*, 3310–3315. [CrossRef]
39. Vempati, S.; Mitra, J.; Dawson, P. One-step synthesis of ZnO nanosheets: A blue-white fluorophore. *Nanoscale Res. Lett.* **2012**, *7*, 470. [CrossRef]
40. Oba, F.; Togo, A.; Tanaka, I.; Paier, J.; Kresse, G. Defect energetics in ZnO: A hybrid Hartree-Fock density functional study. *Phys. Rev. B* **2008**, *77*, 245202. [CrossRef]
41. Rogozin, I.V.; Georgobiani, A.N.; Kotlyarevsky, M.B.; Marakhovskii, A.V. Compensation mechanism for hole conduction in ZnO: N films. *Inorg. Mater.* **2009**, *45*, 391–398. [CrossRef]

Disclaimer/Publisher's Note: The statements, opinions and data contained in all publications are solely those of the individual author(s) and contributor(s) and not of MDPI and/or the editor(s). MDPI and/or the editor(s) disclaim responsibility for any injury to people or property resulting from any ideas, methods, instructions or products referred to in the content.